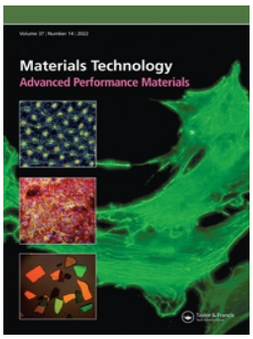

Taylor & Francis
Taylor & Francis Group

Materials Technology
Advanced Performance Materials

ISSN: 1066-7857 (Print) 1753-5557 (Online) Journal homepage: www.tandfonline.com/journals/ymte20

Feasibility study on high-energy-density almost-solid-state sodium batteries with thin ceramic $Na_{3.4}Zr_2Si_{2.4}P_{0.6}O_{12}$ separators

Ansgar Lowack, Rafael Anton, Dörte Wagner, Monika Bhardwaj, Stephan Prünte, Enkhtsetseg Dashjav, Kristian Nikolowski, Frank Tietz, Katja Wätzig, Mihails Kusnezoff, Mareike Partsch & Alexander Michaelis

To cite this article: Ansgar Lowack, Rafael Anton, Dörte Wagner, Monika Bhardwaj, Stephan Prünte, Enkhtsetseg Dashjav, Kristian Nikolowski, Frank Tietz, Katja Wätzig, Mihails Kusnezoff, Mareike Partsch & Alexander Michaelis (2025) Feasibility study on high-energy-density almost-solid-state sodium batteries with thin ceramic $Na_{3.4}Zr_2Si_{2.4}P_{0.6}O_{12}$ separators, Materials Technology, 40:1, 2560836, DOI: 10.1080/10667857.2025.2560836

To link to this article: https://doi.org/10.1080/10667857.2025.2560836

© 2025 The Author(s). Published by Informa UK Limited, trading as Taylor & Francis Group.

Published online: 18 Sep 2025.

Submit your article to this journal

Article views: 299

View related articles

View Crossmark data

Full Terms & Conditions of access and use can be found at
https://www.tandfonline.com/action/journalInformation?journalCode=ymte20

MATERIALS TECHNOLOGY
2025, VOL. 40, NO. 1, 2560836
https://doi.org/10.1080/10667857.2025.2560836

Taylor & Francis
Taylor & Francis Group

OPEN ACCESS Check for updates

Feasibility study on high-energy-density almost-solid-state sodium batteries with thin ceramic $Na_{3.4}Zr_2Si_{2.4}P_{0.6}O_{12}$ separators

Ansgar Lowack[a,b], Rafael Anton[a], Dörte Wagner[a], Monika Bhardwaj[c], Stephan Prünte[c], Enkhtsetseg Dashjav[c*], Kristian Nikolowski[a], Frank Tietz[c], Katja Wätzig[a], Mihails Kusnezoff[a], Mareike Partsch[a] and Alexander Michaelis[a,b]

[a]Fraunhofer Institute of Ceramic Technologies and Systems, Mobile Energy Storage Systems and Electrochemistry, Dresden, Germany; [b]TU Dresden, Institute for Material Science, Chair of Inorganic Non-Metallic Materials, Dresden, Germany; [c]Forschungszentrum Jülich GmbH, Institute of Energy Materials and Devices, IMD-2: Materials Synthesis and Processing, Jülich, Germany

ABSTRACT

This study investigates the feasibility and limitations of almost-solid-state sodium batteries (Na-aSSBs) as novel energy storage solutions. The cell concept comprises a sodium metal anode, a tape-cast $Na_{3.4}Zr_2Si_{2.4}P_{0.6}O_{12}$ solid electrolyte, and a $Na_3V_2(PO_4)_3$ cathode with liquid electrolyte. The impact of the $Na_{3.4}Zr_2Si_{2.4}P_{0.6}O_{12}$ separator and sodium electrode on total cell resistance is evaluated in symmetric Na| $Na_{3.4}Zr_2Si_{2.4}P_{0.6}O_{12}$|Na cells, demonstrating an ultra-low Ohmic resistance below 10 Ωcm^2. The Na-aSSB achieved (85 ± 1) % of the theoretical cathode capacity and energy densities up to (239 ± 10) Wh/l at the cell level, among the highest reported for similar concepts. Cycling stability shows a Coulombic efficiency exceeding 99% over 70 cycles at a 2-h discharge rate. Five performance-limiting factors were identified: initial cathode resistance, degrading cell resistance during cycling, insufficient mechanical strength of the separator, dendrite formation, and non-optimized energy density. Suggested approaches to address these limitations highlight the technological potential of Na-aSSBs.

ARTICLE HISTORY
Received 10 July 2025
Accepted 7 September 2025

KEYWORDS
Almost-solid-state battery; sodium battery; solid electrolyte; tape casting; $Na_{3.4}Zr_2Si_{2.4}P_{0.6}O_{12}$; sodium metal electrode

Introduction

The transition to renewable energy sources is rapidly increasing demand for safe, low-cost and safe energy storage solutions in stationary and mobile applications. Sodium-based batteries with ceramic ion-conducting separators may offer advantages over LIBs: sodium is significantly more abundant compared to lithium; extraction and processing are simpler and less damaging [1]. Ceramic solid electrolytes are non-flammable and therefore have the potential to increase battery safety by reducing the content of flammable liquid electrolytes. However, these benefits remain to be realized. To integrate ceramic solid electrolytes into room temperature battery technology, innovative cell concepts must be explored further to identify and address their critical challenges. This study aims to advance this objective by examining the potential of solid electrolytes in almost solid-state sodium battery (Na-aSSB) model cells at the laboratory scale. This cell concept is conceptually depicted in Figure 1, using 'anode' and 'cathode' designations for the discharge (exothermal) reaction. A comprehensive perspective on related concepts is given by Hasegawa and Hayashi in [2].

For the geometry defined in Figure 1, the cell stack's volumetric energy density (excluding packaging and current collectors) follows as:

$$E_V = \frac{UC_{\text{cathode}}}{A\left(d_{\text{anode}} + d_{\text{cathode}} + d_{\text{separator}}\right)} \tag{1}$$

CONTACT Ansgar Lowack ansgar.lowack@ikts.fraunhofer.de Fraunhofer Institut für Keramische Technologien Und Systeme (IKTS), Winterbergstr 28, Dresden 01277, Germany

*New address: Deutsches Zentrum für Luft- und Raumfahrt e.V. (DLR), Institute of Future Fuels, Solar Chemical Process Development, Linder Höhe, D-51147 Köln, Germany.

© 2025 The Author(s). Published by Informa UK Limited, trading as Taylor & Francis Group.
This is an Open Access article distributed under the terms of the Creative Commons Attribution License (http://creativecommons.org/licenses/by/4.0/), which permits unrestricted use, distribution, and reproduction in any medium, provided the original work is properly cited. The terms on which this article has been published allow the posting of the Accepted Manuscript in a repository by the author(s) or with their consent.

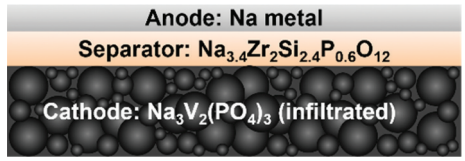

Figure 1. Schematic structure of a Na-aSSB cellFigure 1.

where d_{anode}, $d_{cathode}$ and $d_{separator}$ are the charged-state thicknesses of anode, cathode and separator, A is electrode area, and U is the mean discharge voltage. 'Capacity' C refers to the discharge charge and is limited by the cathode capacity $C_{cathode}$. Thus, $UC_{cathode}$ is the stored energy.

The NASICON-type ceramic $Na_{3.4}Zr_2Si_{2.4}P_{0.6}O_{12}$ serves as both solid electrolyte and separator [3,4]. It is kinetically stable against Na metal at room temperature and reaches 5 mS/cm Na-ion conductivity in bulk samples [4–7]. This value is comparable to liquid electrolytes [8] and exceeds $Li_7La_3Zr_2O_{12}$ (1 mS/cm), the only oxide solid electrolyte directly compatible with Li metal [9]. These traits may enable safer Na-metal anodes by suppressing dendrite growth and avoiding flammable liquids at the anode and separator [10]. Following Equation 1, minimizing the thickness of the solid electrolyte separator ($d_{separator}$) is essential to achieve high energy density. Herein leighs the principal novelty of the presented work which uses very thin, tape-cast $Na_{3.4}Zr_2Si_{2.4}P_{0.6}O_{12}$ separators with 50–110 µm thickness [11,12] in the full cell. While studies on cell concepts similar to Figure 1 exist and address central challenges with innovative and promising approaches such as [13–19], they use substantially thicker, pellet-type $Na_{3.4}Zr_2Si_{2.4}P_{0.6}O_{12}$ separators leading to markedly lower energy density. Tape-cast reports with thinner separators [20–23] likewise achieved lower energy density, as only thicker tapes were used, or additional ceramic host were utilized in the metal anode which, while solving critical interfacial issues, reduce energy density.

On the anode side, metallic sodium is used. In the absence of a liquid electrolyte at the Na|ceramic interface, intimate and stable contact is essential [24–26]. Poor contact causes current constriction and large resistances [5,27–31], producing high local current densities that promote dendrite penetration and failure during charging [32–35]. Stripping/plating can be partly irreversible due to small Na losses during cycling [27,29], necessitating excess Na relative to $C_{cathode}$. Press-lamination of Na foil at 10 MPa has previously been shown to achieve good contact and low interfacial resistance (<2 $\Omega\cdot cm^2$) on thick substrates [29]. Although this method is, in principle, applicable to thin tapes with sufficient mechanical integrity [36], implementing isostatic pressure to compensate for residual warping from sintering is technologically challenging. As an alternative, this study adapts an ultrasonic sonotrode process to contact Na with thin $Na_{3.4}Zr_2Si_{2.4}P_{0.6}O_{12}$ substrates [37].

For the cathode, $Na_3V_2(PO_4)_3$ is synthesized by a wet-chemical route [38] and used as active material [39,40]. It exhibits a 3.4 V plateau vs Na via the V^{III}/V^{IV} couple:

$$Na_3V_2^{III}(PO_4)_3 Na_{3-x}V_{2-x}^{III}V_x^{IV}(PO_4)_3 + xNa^+ + xe^- \quad (2)$$

Carbon coating of the active material particles mitigates their intrinsically low electronic conductivity in the µS/cm-range [41]. Although $Na_3V_2(PO_4)_3$ shows promising cycling stability [42], vanadium raises availability [43] and toxicity [44] concerns; for future implementation, less critical cathodes such as Prussian blue analogues [45] and selected layered oxides [46] should be explored. The solid-state concept is not extended into the cathode: unavoidable porosity, microcracks, and tortuosity would limit ionic transport and rate capability relative to a liquid-filled microstructure. Instead, an auxiliary liquid electrolyte is infiltrated into the cathode porosity, completing the aSSB setup [47,48]. While metallic sodium remains flammable, the absence of additional flammable liquids in the anode and separator reduces fire hazard.

The following sections detail laboratory-scale fabrication of the model cells and their components and evaluate electrochemical performance and the high-energy-density potential enabled by very thin tape-cast $Na_{3.4}Zr_2Si_{2.4}P_{0.6}O_{12}$ separators.

Experimental section

$Na_3V_2(PO_4)_3$ synthesis

$Na_3V_2(PO_4)_3$ was prepared using citric acid as chelating agent. Appropriate amounts of NaH_2PO_4 (Sigma Aldrich, ≥99.0%), NH_4VO_3 (Merck, ≥99.0%), and citric acid monohydrate (Merck, ≥99.5%) were dissolved under constant stirring in a beaker filled with 150 ml H_2O and 30 ml ethanol. The resulting blue solution was dried overnight at 80°C. The gained solid was crushed in an agate mortar and subsequently milled in a high energy planetary mill (Retsch PM400) at 250 rpm using ethanol-filled ZrO_2 containers and ZrO_2 balls. After drying, the powder was calcinated at 300°C and milled again using the same device and parameters as before. Finally, the powder was reduced at 800°C in Ar/H_2 (2.9 vol%). For evaluation of the electrochemical performance of the synthesized $Na_3V_2(PO_4)_3$, coin cells with organic liquid electrolyte were assembled. The $Na_3V_2(PO_4)_3$ powder was mixed with a polyvinylidene fluoride binder (PVDF) and Super P as conductive additive in mass ratio of 80:10:10. For a homogeneous cathode paste, first the binder was dissolved in N-methyl-2-pyrrolidone (NMP) in a planetary centrifugal mixer (Thinky Corp., Japan) at 1000 rpm and then Super P and $Na_3V_2(PO_4)_3$ were added one after the other and mixed for 2 min each time. The cathode paste was coated on aluminium foil using a bar coater and subsequently dried in a vacuum drying oven at 80°C. After drying, 10 mm disks were cut and assembled into coin cells using a glass fibre separator, 1 M $NaPF_6$ in polycarbonate with 2 wt% fluoroethylene carbonate as liquid electrolyte (50 µl) and sodium metal as anode.

Fabrication and application of $Na_3V_2(PO_4)_3$ cathodes

For the aSSB-approach, $Na_3V_2(PO_4)_3$ powder (92.5 wt%) was blended with carbon black (Super C65, 5 wt%) and a PVDF binder (2.5 wt%) in NMP to create a homogenous slurry. This slurry was then coated onto aluminium foil and subsequently dried. Circular electrodes (diameter 5–8 mm) were cut from the dried foils and transferred to a hydraulic press, where they were densified using a suitable steel spacer to attain the desired thickness. Two different cathode thicknesses were fabricated: one with a mass loading of 11.9 mg/cm^2, corresponding to a capacity of 1.30 mAh/cm^2 and a thickness of (100 ± 10) µm, and another with a mass loading of 23.1 mg/cm^2, yielding a capacity of 2.52 mAh/cm^2 and a thickness of (200 ± 10) µm. In both cases, a theoretical capacity for $Na_3V_2(PO_4)_3$ of 118 mAh/g is assumed (following from the stoichiometry of the material). The gravimetric densities were (3.2 ± 0.1) g/cm^3 for $Na_3V_2(PO_4)_3$, (1.75 ± 0.05) g/cm^3 for PVDF and (2.0 ± 0.1) g/cm^3 for Super C65. The dry cathode therefore has an average density of the solid components of (3.05 ± 0.08) g/cm^3 and a porosity of approximately 63%.

Synthesis of $Na_{3.4}Zr_2Si_{2.4}P_{0.6}O_{12}$

The $Na_{3.4}Zr_2Si_{2.4}P_{0.6}O_{12}$ powder was synthesized using a solution-assisted solid-state reaction method [4,49]. $NaNO_3$ (VWR), $ZrO(NO_3)_2$ (Aldrich), $Si(OCH_2CH_3)_4$ (Merck), and $NH_4H_2PO_4$ (Merck) were used as analytically pure starting materials. Stoichiometric amounts of $NaNO_3$ and $ZrO(NO_3)_2$ were dissolved in deionized water. A stoichiometric amount of $Si(OCH_2CH_3)_4$ was also added to the solution while stirring. After hydrolysis of $Si(OCH_2CH_3)_4$, $NH_4H_2PO_4$ was added to the system during stirring. Immediately a precipitation of complex zirconium oxyphosphate compounds was formed. The whole mixture was dried at 85°C and then calcined at 800°C for 3 h. After calcination, a white powder was obtained which was then milled in 96% ethanol with zirconia balls on a milling bench for 48 h and dried at 70°C for 12 h.

Fabrication of thin $Na_{3.4}Zr_2Si_{2.4}P_{0.6}O_{12}$ substrates via tape casting

For the fabrication of thin ceramic layers from the calcined $Na_{3.4}Zr_2Si_{2.4}P_{0.6}O_{12}$ powder, the tape casting process was used and alcohol-based suspensions were developed [50]. An azeotropic mixture of ethanol (67 vol.%) and methyl ethyl ketone (33 vol.%) was chosen as organic solvent to which organic additives such as polyvinyl butyral as a binder and triethyleneglycol bis (2-ethyl hexanoate) and polyethylene glycol as

plasticizers were added to stabilize the suspension. As dispersing agent, a steric stabilizing copolymer containing multiple-adsorbing anchoring groups was chosen, which is compatible with the binder and plasticizer. To obtain a homogeneous dispersion, the slurry was mixed in a planetary mixer at 1500 rpm for 8 min and continuously ball-milled for 12 h. To eliminate bubbles, the slurry was degassed by stirring in a vacuum chamber for 2 h.

The slurry was tape-cast on a polymeric foil to obtain a layer of about 80 µm or 150 µm. Samples with a diameter of 14 mm were punched out of the tape-cast green tape via a punching tool. The green tapes were sintered in a muffle furnace (RWF 1200, Carbolite Gero GmbH & Co. KG, Germany) in ambient atmosphere. To achieve thin and planar samples, the green tapes were placed between two pellets consisting of the same $Na_{3.4}Zr_2Si_{2.4}P_{0.6}O_{12}$ material. The sintering procedure consists of two steps: during the initial step the organics were removed from the green tapes and during the second step the powder was densified. At the beginning, the heating rate was 30 K/h followed by a dwell time of 2 h at 600°C to guarantee a complete removal of the organic compounds. Afterwards the samples were sintered at 1250°C for 4 h, whereby the heating rate was 180 K/h. The cooling rate was set to 30 K/h. The resulting tapes had a thickness of 50 µm or 110 µm, respectively.

Application of sodium metal anodes

Inside an argon-filled glove box, a (36 ± 5) µm thick sodium metal foil was prepared by pressing sodium metal onto aluminium foil at 97°C using a heated press. Circular electrodes with diameters of 8 mm were cut from the foil and positioned onto the $Na_{3.4}Zr_2Si_{2.4}P_{0.6}O_{12}$ tapes. The sodium foil was then carefully placed using plastic tweezers without applying significant pressure and placed on a heating plate at 97°C. An ultrasonic sonotrode (Hielscher UP200St, 50W, 50% amplitude) was employed to gently apply pressure to the sodium film from above. To assemble symmetric cells, this procedure was performed on both sides of the $Na_{3.4}Zr_2Si_{2.4}P_{0.6}O_{12}$sample. For cells which were pressurized at 1 MPa, $Na_{3.4}Zr_2Si_{2.4}P_{0.6}O_{12}$ substrates with next to no warping are required to avoid fracture of the separator. To achieve this, the largest and most planar shards of $Na_{3.4}Zr_2Si_{2.4}P_{0.6}O_{12}$ tapes were selected that previously broke during uniaxial compression. Circular sodium electrodes with diameters of 5 mm were applied to these shards, using the same contacting method.

For the full cell, this sodium layer relates to the thickness of the anode in the discharged state. During charging, this thickness increases by 8.83 µm per 1mAh/cm^2 of charge (based on the properties of sodium metal: C_{Na} = 1166 mAh/g and ρ_{Na} = 0.968 g/cm^3).

Cell assembly and electrochemical methods

The separator with the sodium metal anode was placed onto a graphite spacer of appropriate size inside of a pressure-adjustable and inertly sealable test cell (EL-CELLs Pat-Core-Force system) with the sodium side at the bottom. The upwards-positioned side was wetted with liquid electrolyte (1 M $NaClO_4$ in ethylene carbonate/propylene carbonate PC:EC, 1:1 by weight). The cathode foil was soaked in the same liquid electrolyte for about an hour to achieve a complete infiltration. The cathode foil was then positioned on the liquid electrolyte-wetted $Na_{3.4}Zr_2Si_{2.4}P_{0.6}O_{12}$ surface, and the structure was blotted dry from above to remove excess liquid electrolyte. A second graphite spacer was placed on the cell stack. Subsequently, the test cell housing was sealed. The pressure on the cell was slowly and uniaxially applied and measured before and after the electrochemical characterization. The assembled cells were transferred to a temperature-controlled chamber outside the glovebox. Electrochemical measurements were carried out with a four-wire method, using a VMP-3 Biologic potentiostate. To characterize the $Na_{3.4}Zr_2Si_{2.4}P_{0.6}O_{12}$ tapes with symmetric sodium electrodes, impedance spectra were recorded at frequencies between 1 MHz and 1 Hz at temperatures between −10°C and 40°C. In the following, the term 'formation' refers to the initial charging and discharging of a battery at low current densities, to form conductive pathways at lower stress (e.g. due to volume changes). By this convention, full cells were subjected to four formation cycles, by charging to 3.8 V cell voltage and discharging to 2.6 V at 30°C, repeatedly, in both cases at a constant current density approximately equivalent to charging or discharging of the cell in 10 h. Subsequent cycling was carried out within the same voltage limits, but at higher current densities. Before and after formation, and after every 10 cycles, full cells were investigated by impedance spectroscopy at frequencies between 1 MHz and 0.1 Hz.

Results and discussion

Electrochemical characterization of $Na_3V_2(PO_4)_3$

At room temperature, the cycling properties of coin cells with $Na_3V_2(PO_4)_3$ cathodes were stable reaching 99 mAh/g at currents equivalent to charge and discharge in 10 h (C/10). This value corresponds to 85% of the theoretical active material capacity of 118 mAh/g (following from the stoichiometry of the material). Cells exhibit high cycling stability, retaining 98% of the 99 mAh/g over 500 cyles (Figure 2). It can be concluded that degradation of the active material particles during charging and discharging can be neglected as a mechanism of cell degradation below 500 cycles. The results are in very good agreement with similar cells reported previously [42].

Characterization of the $Na_{3.4}Zr_2Si_{2.4}P_{0.6}O_{12}$ substrates

The phase composition of the solid electrolyte tapes was investigated via X-ray diffractometry after sintering. As depicted in Figure 3 the diffractogram shows that the desired sodium conductive NaSICON phase $Na_{3.4}Zr_2Si_{2.4}P_{0.6}O_{12}$ is the main phase of the substrates. The steps and processes leading to this optimized composition were previously discussed in detail [51,52].

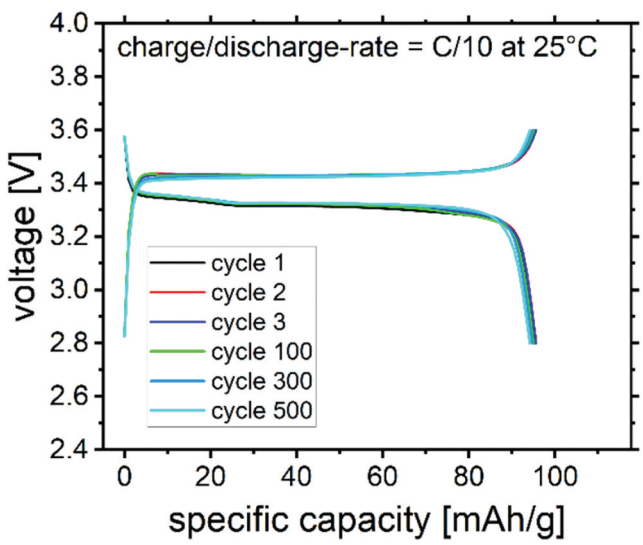

Figure 2. Galvanostatic curves (500 cycles) of the $Na/Na_3V_2(PO_4)_3$ cell. Charge normalized to active material mass.

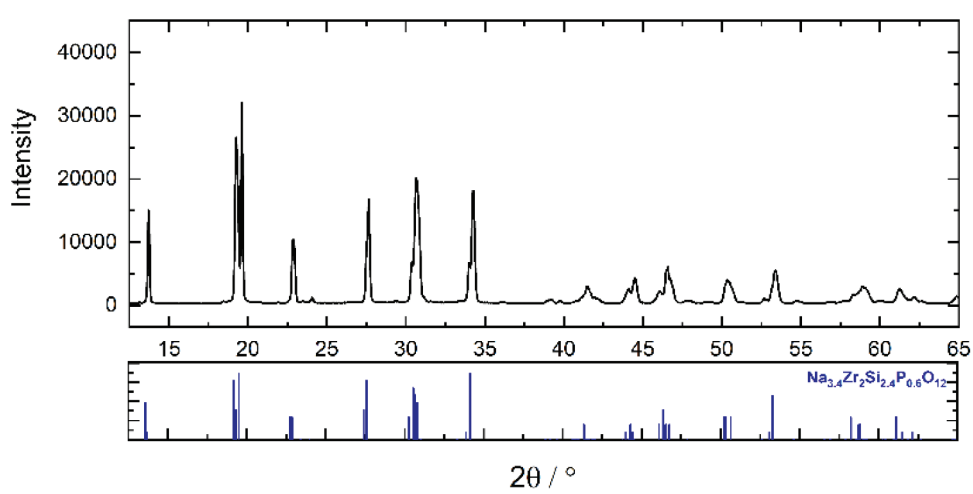

Figure 3. XRD of $Na_{3.4}Zr_2Si_{2.4}P_{0.6}O_{12}$ – solid electrolyte after sintering.

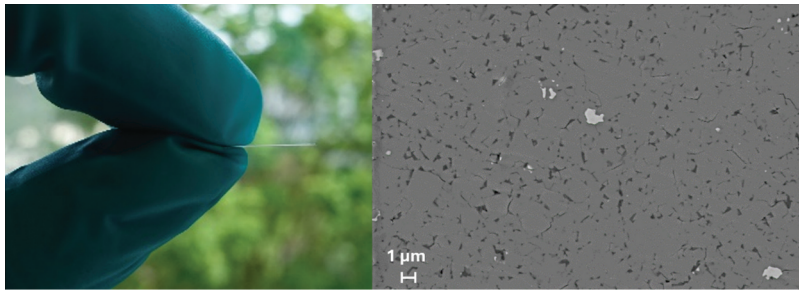

Figure 4. 110 µm thin $Na_{3.4}Zr_2Si_{2.4}P_{0.6}O_{12}$ foil and corresponding SEM image of polished cross-section.

Figure 4 shows a 110 µm thin $Na_{3.4}Zr_2Si_{2.4}P_{0.6}O_{12}$ substrate (left) and its polished cross-section (right). As can be seen in the left image, the samples are plane and have sufficient mechanical stability to be handled manually. The SEM image (right) reveals a microstructure with a porosity of (4.1 ± 0.5) %, distributed homogenously throughout the sample in the form of small pores. Besides the main phase $Na_{3.4}Zr_2Si_{2.4}P_{0.6}O_{12}$ there are few ZrO_2 (identified via EDX-probing) particles visible as white spots in the cross-section. Most likely, ZrO_2 was formed due to incomplete reactions during synthesis, stoichiometric deviations in the precursor materials or thermal decomposition during sintering. In addition to the pores, some microcracks at grain boundaries between sintered particles are observed as bulk defects, which most likely contribute to an increased probability for dendrite formation [34].

Electrochemical characterization of the $Na_{3.4}Zr_2Si_{2.4}P_{0.6}O_{12}$ separators and the Na| $Na_{3.4}Zr_2Si_{2.4}P_{0.6}O_{12}$ interface

For the determination of the sodium conductivity of the $Na_{3.4}Zr_2Si_{2.4}P_{0.6}O_{12}$ tapes and the degree of Ohmic resistance limitation caused by the Na| $Na_{3.4}Zr_2Si_{2.4}P_{0.6}O_{12}$ interface in the full cell, impedance spectra between 1 MHz and 1 Hz were measured in symmetric Na| $Na_{3.4}Zr_2Si_{2.4}P_{0.6}O_{12}$|Na test cells with 110 µm thick separator at temperatures between −10°C and 40°C. The results of one exemplary cell are depicted in Figure 5(a).

The impedance spectra of Na| $Na_{3.4}Zr_2Si_{2.4}P_{0.6}O_{12}$|Na cells consist of four different impedance contributions at different frequencies [5,31]:

(A) At high frequencies, the resistance and polarization of the individual $Na_{3.4}Zr_2Si_{2.4}P_{0.6}O_{12}$ grains can be observed. This process was observed by Ortmann et al. for $Na_{3.4}Zr_2Si_{2.4}P_{0.6}O_{12}$ at frequencies above 1 MHz, even at temperatures as low as −40°C [5].
(B) Polarization of grain boundaries contributes at intermediate frequencies. This phenomenon is highly specific to the sintering conditions of the solid electrolyte.
(C) Also at intermediate frequencies, the Na| $Na_{3.4}Zr_2Si_{2.4}P_{0.6}O_{12}$ interfaces cause an impedance due to the $Na_{3.4}Zr_2Si_{2.4}P_{0.6}O_{12}$ heterogeneous points of electrochemical contact between both materials and current constriction to these points [5,29].
(D) At low frequencies, a slight increase in impedance is usually observed. Its origin is however not fully understood [5,27].

Two distinct maxima in the impedance spectra are apparent in Figure 5(a) below 1 MHz and are assigned to the two processes at intermediate frequencies, i.e. grain boundaries (contribution B) and Na| $Na_{3.4}Zr_2Si_{2.4}P_{0.6}O_{12}$ interfaces (contribution C). The low-frequency contribution D is observed below frequencies of 90 Hz at −10°C and shifted to higher frequencies with increasing temperature (marked in Figure 5(a)). The spectra are therefore fitted at frequencies above the transition to contribution D by the equivalent circuit shown in Figure 5(a).

The two contributions B and C are fitted with two parallel circuits, connected in series, each consisting of a real areal resistance R_B or R_C and a constant phase element CPE_A or CPE_B with fit parameters Q and n and impedance Z_{CPE}:

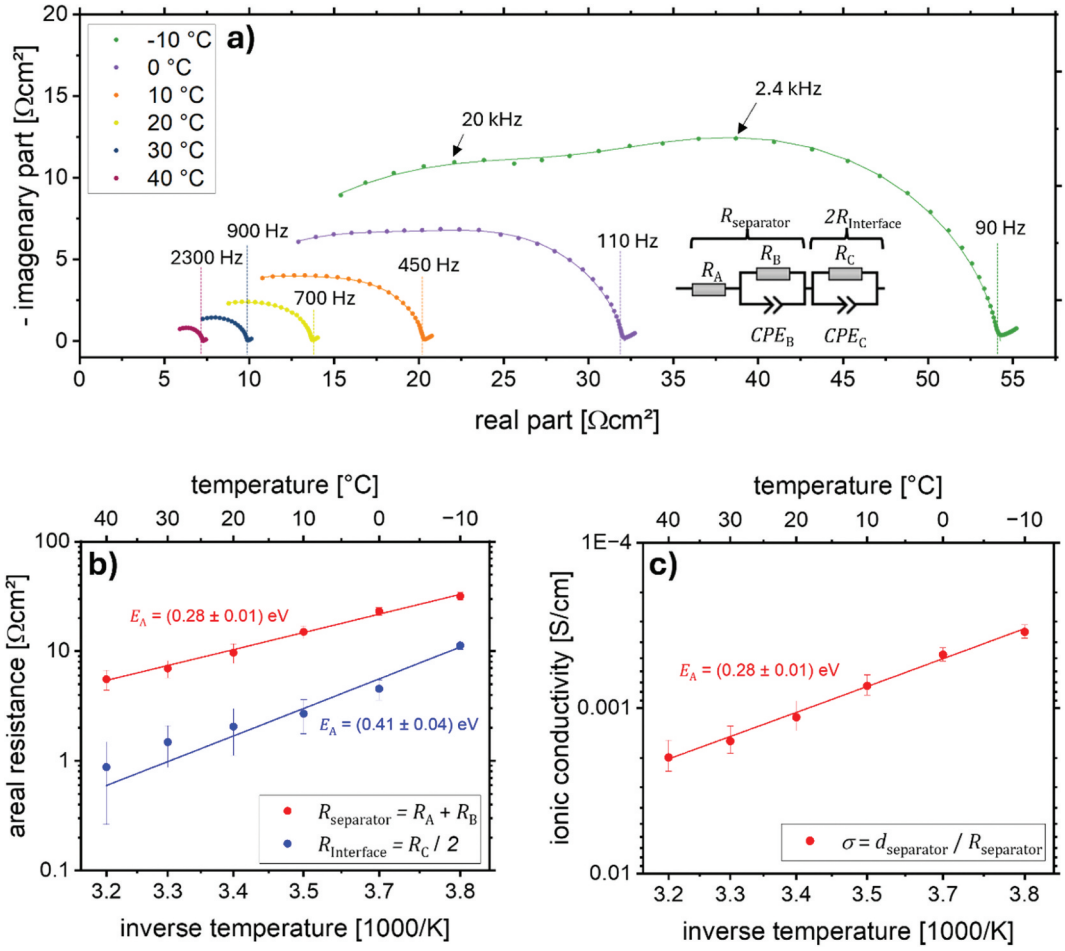

Figure 5. (a) Impedance spectra of a Na| $Na_{3.4}Zr_2Si_{2.4}P_{0.6}O_{12}$|Na cell with a 110 µm thin $Na_{3.4}Zr_2Si_{2.4}P_{0.6}O_{12}$ separator at different temperatures and the equivalent circuit for fitting the spectra. b) Areal resistances of $Na_{3.4}Zr_2Si_{2.4}P_{0.6}O_{12}$ and the Na| $Na_{3.4}Zr_2Si_{2.4}P_{0.6}O_{12}$ interface with fit to Arrhenius equation. c) ionic conductivity of $Na_{3.4}Zr_2Si_{2.4}P_{0.6}O_{12}$ tape with fit to Arrhenius equation (Equation 4 in the text).

$$Z_{CPE}(f) = \frac{1}{Q(2\pi i f)^n}. \tag{3}$$

The model is adjusted with a third areal resistance R_A connected in series, to attribute for unresolved high-frequency contributions (e.g. grain polarization, contribution A). Since the grain polarization is not resolved, separation of grain and grain boundary contributions was not possible. Instead, the Ohmic resistance $R_{separator}$ of the $Na_{3.4}Zr_2Si_{2.4}P_{0.6}O_{12}$ separator is calculated as the sum of R_A and R_B and plotted in Figure 5(b) for all temperatures. The Ohmic resistance $R_{Interface}$ assigned to each of the two interfaces is plotted as $R_C/2$. For future reference, the volume specific ionic conductivity $\sigma = d_{separator}/R_{separator}$ is plotted in Figure 5(c) ($d_{separator} = 110$ µm). To determine the activation energies E_A of ionic transport, the data points are fitted to an inverse Arrhenius equation:

$$R = T\kappa \exp\left(\frac{E_A}{k_B T}\right), \tag{4}$$

where k_B denotes the Boltzmann's constant, T the absolute temperature and κ a material-dependent constant (for Figure 5(c) the reciprocal of Equation 4 applies).

For the scope of this study, it is concluded that the Ohmic resistance of one Na| $Na_{3.4}Zr_2Si_{2.4}P_{0.6}O_{12}$ interface and the $Na_{3.4}Zr_2Si_{2.4}P_{0.6}O_{12}$ separator will together contribute less than 10 Ωcm^2 to the aSSB cell resistance at 30°C. Therefore, any resistance of the aSSB beyond 10 Ωcm^2 will be attributed to the cathode or the cathode| $Na_{3.4}Zr_2Si_{2.4}P_{0.6}O_{12}$ interface.

The $Na_{3.4}Zr_2Si_{2.4}P_{0.6}O_{12}$ separator exhibits an ionic conductivity of $\sigma = (1.6 \pm 0.3)$ mS/cm at 30°C and (1.3 ± 0.3) mS/cm at 25°C. For comparison, Ma et al. measured values as high as 5 mS/cm at 25°C in bulk pellet-type $Na_{3.4}Zr_2Si_{2.4}P_{0.6}O_{12}$ samples of the same composition ($Na_{3.4}Zr_2Si_{2.4}P_{0.6}O_{12}$) [4]. Process-related differences influencing the microstructure, such as different green density and the use of organics for tape casting, may result in slightly deviating particle arrangements and grain sizes. Therefore, the likely reasons for this deviation are pores and microcracks at grain boundaries visible in Figure 4. With decreasing frequency, the ionic current will be increasingly constricted to surfaces of good geometric contact between grains. The grain boundary resistance normalized to these surfaces of good geometric contact due to orientation changes or glassy phases between grains will be significantly lower than R_B. As discussed by Eckhardt et al. [5,30,31], the linear equivalent circuit shown in Figure 5(a) fails to accommodate for this three-dimensional effect. The hypothesis that not grain boundary areal resistance but rather the geometric contact between grains limits overall conductivity of the $Na_{3.4}Zr_2Si_{2.4}P_{0.6}O_{12}$ tapes, is supported by the finding, that the activation energy of (0.28 ± 0.01) eV does not differ significantly from the values reported by Ma et al. [4], in contrast to the overall conductivity. Should secondary phases between grains contribute significantly to overall $Na_{3.4}Zr_2Si_{2.4}P_{0.6}O_{12}$ resistivity, a significant deviation in activation energy would be expected. Consequently, the $Na_{3.4}Zr_2Si_{2.4}P_{0.6}O_{12}$ tapes still show potential for higher ionic conductivity by further optimization of the microstructure. However, as will be discussed below, the resistance of the full cells is significantly higher than 10 Ωcm^2 due to limitations in the cathode. Therefore, from a resistance perspective, optimizing the microstructure of the separators and reducing secondary phases would not provide significant advantages.

The Na| $Na_{3.4}Zr_2Si_{2.4}P_{0.6}O_{12}$ interface contribution ($R_{Interface}$) is (1.5 ± 0.6) Ωcm^2 at 30°C and (1.8 ± 0.8) Ωcm^2 at 25°C. These values do not deviate significantly from the interfacial resistance of about 1 Ωcm^2 reported by Ortmann et al. [5] which was attributed to the decomposition of $Na_{3.4}Zr_2Si_{2.4}P_{0.6}O_{12}$ when in contact with sodium metal. This finding indicates good geometric contact between sodium metal and $Na_{3.4}Zr_2Si_{2.4}P_{0.6}O_{12}$, since lacklustre geometric contact would result in significantly larger interfacial resistance contributions due to purely geometric effects (discussed in detail by Eckhardt et al. in [31]). However, the similarity in activation energy between the interface (0.41 ± 0.04) eV and the bulk (0.28 ± 0.01) eV of the $Na_{3.4}Zr_2Si_{2.4}P_{0.6}O_{12}$ separator is not large enough to exclude that dynamic current constriction contributes to the observed value of $R_{Interface}$. Fitting $R_{Interface}$ to Equation 4 is therefore not without uncertainty and the temperature dependence of the resistance between sodium metal and $Na_{3.4}Zr_2Si_{2.4}P_{0.6}O_{12}$ warrants further studies.

Cycling of $Na_3V_2(PO_4)_3/Na_{3.4}Zr_2Si_{2.4}P_{0.6}O_{12}$/Na full cells

aSSBs were assembled using metallic sodium anodes, thin $Na_{3.4}Zr_2Si_{2.4}P_{0.6}O_{12}$ separators, and liquid electrolyte-infiltrated $Na_3V_2(PO_4)_3$ cathodes as described in the experimental section. However, the fabrication process on laboratory scale remained non-optimized resulting in a low production yield due to the fracture of the brittle $Na_{3.4}Zr_2Si_{2.4}P_{0.6}O_{12}$ tapes during assembly. Consequently, this paper focuses on the cell with the highest energy density (cell 1 in the following) and the one with the best cycling stability (cell 2). The primary objective is to provide a proof of concept and to identify the fundamental limitations of the cell design. The specifications and electrochemical performances of both cells are summarized in Table 1 and will be discussed in the following.

The volumetric densities E_V are calculated from Equation 1. With the cathode porosity of $P = (63 \pm 3)\%$ and the densities $\rho_{Na} = 0.968$ g/cm^3 (sodium metal), $\rho_{solid\ electrolyte} = (3.3 \pm 0.1)$ g/cm^3 ($Na_{3.4}Zr_2Si_{2.4}P_{0.6}O_{12}$ separator), $\rho_{cathode} = (3.05 \pm 0.08)$ g/cm^3 (solid cathode components), and $\rho_{liquid} = (1.38 \pm 0.02)$ g/cm^3 (liquid electrolyte), the gravimetric energy densities E_m are calculated as

$$E_m = \frac{UC_{cathode}}{A\left\{\rho_{Na}d_{anode} + \rho_{solid\ electrolyte}d_{separator} + \left[(1-P)\rho_{cathode} + P\rho_{liquid}\right]d_{cathode}\right\}}. \quad (5)$$

The highest energy density was reached in cell 1 with a theoretical cathode capacity of $C_{Cathode,\ theo} = 2.52$ mAh/cm^2, a cathode thickness of $d_{cathode} = (200 \pm 10)$ µm, an anodic sodium layer thickness of $d_{anode} = (55 \pm 6)$ µm in the charged state and a $d_{separator} = (50 \pm 4)$ µm thick $Na_{3.4}Zr_2Si_{2.4}P_{0.6}O_{12}$ separator. A voltage

Table 1. Summary of parameters for cell 1 and cell 2. All quantities refer to the charged cells. Volume expansion of active material is insignificant compared to geometric measurement errors.

Quantity	unit	Cell 1	Cell 2
Anodic sodium reservoir layer	µm	36 ± 5	36 ± 5
Charged anode thickness d_{anode}	µm	55 ± 6	47 ± 6
Separator thickness $d_{separator}$	µm	50 ± 4	110 ± 5
Cathode thickness $d_{cathode}$	µm	200 ± 10	100 ± 10
External pressure	MPa	0.005 ± 0.002	1.0 ± 0.1
Theo. charge $C_{cathode,\ theo}$	mAh/cm^2	2.52	1.32
Real charge $C_{cathode,\ real}$	mAh/cm^2	2.14	1.11
Vol. theo. energy density $E_{V,\ theo}$	Wh/l	277 ± 11	174 ± 9
Vol. real energy density $E_{V,\ real}$	Wh/l	239 ± 10	148 ± 7
Grav. theo. energy density $E_{m,\ theo}$	Wh/kg	138 ± 6	74 ± 4
Grav. real energy density $E_{m,\ real}$	Wh/kg	118 ± 5	62 ± 3
Formation cycles at C/10	–	4	4
Cycles at C/2	–	–	70

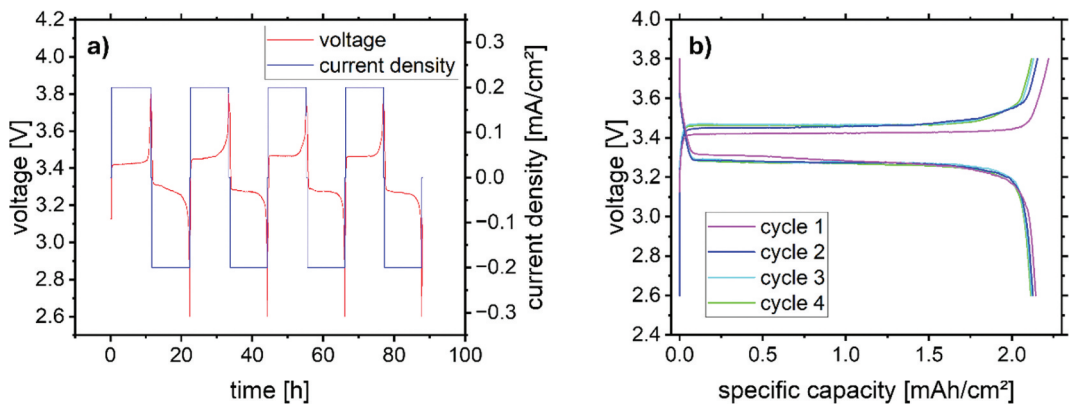

Figure 6. (a) Voltage and current density during formation cycles of high-capacity Na-aSSB (cell 1) at 0.2 mA/cm^2 (C/10), b) voltage vs. charge during the same measurement.

plateau of 3.4 V results in theoretical energy densities of $E_{V,\ theo}$ = (277 ± 11) Wh/l and $E_{m,\ theo}$ = (138 ± 6) Wh/kg. The cell was charged and discharged at j = 0.2 mA/cm^2 (approximately C/10) for four formation cycles between 2.6 V and 3.8 V, as depicted in Figure 6(a,b).

Initially, the cell is charged to 2.21 mAh/cm^2. The first discharge yields 2.14 mAh/cm^2, i.e. 97% of the charge is recovered compared to the first charging of the cell, corresponding to energy densities of $E_{V,\ real}$ = (238 ± 10) Wh/l and $E_{m,\ real}$ = (118 ± 5) Wh/kg. These values correspond to 85% of the theoretical capacity of the $Na_3V_2(PO_4)_3$ in the cathode. The following three formation cycles all recover more than 98% of the charge during discharge. Cell resistance was found to be notably high and increased further during formation cycling (Figure 7(a)). With a DC resistance of more than 500 Ωcm^2, the Ohmic voltage drop at significant current densities (e.g. j = 1 mA/cm^2, approximately equivalent to C/2) is too high (>0.5 V) to cycle the cell between 2.6 V and 3.8 V without significant energy loss due to Joule heating.

Figure 7(a) shows the impedance spectra before and after the four formation cycles. By comparison with Figure 5, it is apparent that both impedance spectra are dominated by the cathode contribution. The smaller impedance contribution of the $Na_{3.4}Zr_2Si_{2.4}P_{0.6}O_{12}$ tape and its interface to the sodium metal electrode is concealed by other larger contributions in the spectrum of the full cell. In both spectra, before and after formation, the capacitive rise at low frequencies below 1 Hz is attributed to the cathodic current collector and its increasingly blocking behaviour. It is modelled by the right CPE_{CC} in the equivalent circuit depicted in Figure 7(a). A minimum in imaginary impedance (or maximum in the absolute value of the imaginary part) at about 10 Hz in both spectra of cell 1 is attributed to ion diffusion in the liquid electrolyte and fitted by a parallel circuit containing a real resistance R_{LE} and a second CPE_{LE}. Finally, with an imaginary minimum at 1500 Hz before formation and 230 Hz after formation, the largest impedance contribution is found in both spectra and fitted by another parallel circuit of a real resistance R_{CT} and a third CPE_{CT}. This semicircle increases significantly during the

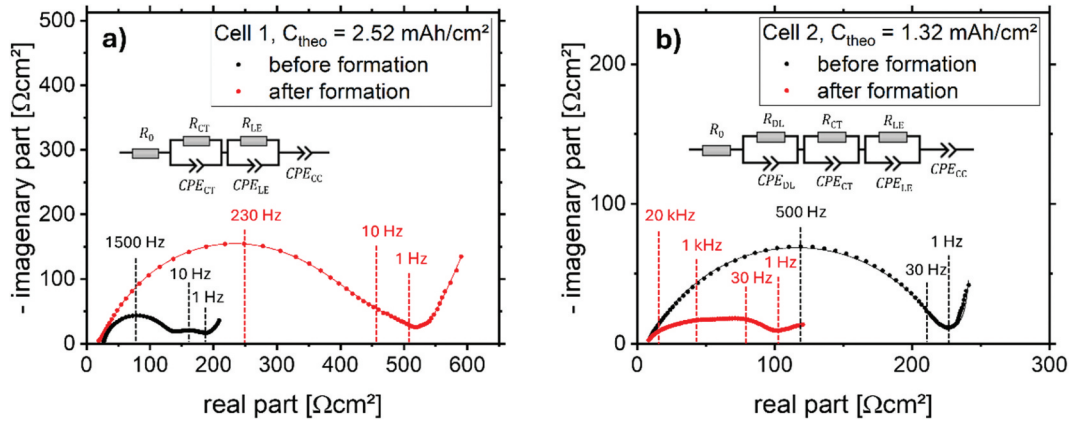

Figure 7. Impedance spectra of cells before and after formation at 30°C; to achieve detailed visualization, a) and b) are differently scaled. a) high-capacity cell 1 at low pressure (0.05 MPa), b) low-capacity cell 2 at high pressure (1 MPa). Spectra were fitted with the inserted equivalent circuits to assign low frequency polarization due to the cathodic current collector (CC), liquid electrolyte diffusion (LE), cathodic charge transfer impedance (CT) and the impedance of the electrochemical double layer (DL). Any unresolved processes above 1 MHz are modeled with a resistor R_0.

formation cycles and indicates an increase in the charge transfer resistance at the electrode surface due to changes in the electrode structure. An alternative hypothesis for this semicircle increase would be a chemical interphase formation between either $Na_{3.4}Zr_2Si_{2.4}P_{0.6}O_{12}$ and liquid electrolyte or active material and liquid electrolyte. However, as will be discussed in the following, this explanation is unlikely, since similar degradation was not observed when applying increased external pressure during cell formation.

The cell 1 presented in Figures 6 and 7(a) was assembled and characterized at low external pressure (approximately 0.05 MPa). An increase of uniaxial pressure to cells with 50 µm thin $Na_{3.4}Zr_2Si_{2.4}P_{0.6}O_{12}$ separators consistently led to fracture of the ceramic tape. Therefore, the geometry of components was altered to increase mechanical and cycling stability. The most stable cycling performance was achieved in cell 2 with a theoretical cathode capacity of 1.32 mAh/cm^2 at a cathode thickness of (100 ± 10) µm, an anodic sodium layer thickness of d_{anode} = (47 ± 6) µm in the charged state and a $d_{separator}$ = (110 ± 5) µm thick $Na_{3.4}Zr_2Si_{2.4}P_{0.6}O_{12}$ separator. Thus, in comparison to cell 1, the cathode capacity and thickness were roughly halved to improve reaction kinetics, following the discussed observation that full cell impedance is dominated by the cathode. The separator was roughly doubled in thickness, because even with this thickness it does not significantly contribute to cell resistance (as reported in Figure 5). The thicker separator was sufficiently strong to prevent fracture (albeit not consistently) when significant uniaxial pressure of 1 MPa was applied during cell assembly and kept at 1 MPa during the electrochemical characterization as confirmed by the force measurement of the test cell housing. However, based on these changes, the theoretical energy densities of cell 2 are only $E_{V,\ theo}$ = (174 ± 9) Wh/l and $E_{m,\ theo}$ = (74 ± 4) Wh/kg, significantly lower than for cell 1.

Again, four formation cycles were carried out with cell 2. The impedance spectra recorded before and after the formation cycles are depicted in Figure 7(b). In contrast to cell 1 with thicker electrode and without significant applied pressure (Figure 7(a)), a significant decrease in total cell resistance was observed during formation. After formation, a total resistance of 120 Ωcm^2 was measured at 0.1 Hz for cell 2, compared to 590 Ωcm^2 for cell 1. Before formation, both cells exhibited similar total resistances of around 230 Ωcm^2 at 0.1 Hz. This observation regarding the pre-formation measurements is unexpected, as the thicker cathode in cell 2 would typically suggest a higher resistance. However, this discrepancy should not be overinterpreted, as the conductive pathways in the cathode after cell assembly can be significantly affected by surface contaminations at the interfaces between components. Consequently, the comparison of different cells before formation is difficult.

In contrast, comparing the impedance spectra of the same cells before and after formation is valuable because it allows to assess how the electrochemical properties and conductive pathways develop during the formation process, e.g. by the decomposition of contaminations at the interfaces during SEI-formation. This analysis provides insights into the extent to which the formation affects the performance of an individual cell.

Comparing the impedance spectra of different cells after formation is also meaningful because, at this point, the conductive pathways will be stable and variations in surface contaminations of the different components will be gone due to SEI formation. This allows for a more accurate comparison between different cells.

As before in Figure 7(a), the contributions in Figure 7(b) at frequencies below 1 Hz are attributed to polarization due to the cathodic current collector and modelled as CPE_{CC} (see right-hand side of the equivalent circuit in Figure 7(b)). The maximum in the absolute value of the imaginary part which was attributed in Figure 7(a) to ionic diffusion in the liquid electrolyte is again found in Figure 7(b) after formation at about 30 Hz and is modelled as before with the parallel circuit containing a real resistance R_{LE} and a second CPE_{LE} (first from the right). Prior to formation such a maximum is less visible due to the much larger contribution with a minimum imaginary impedance at 500 Hz. The latter is modelled by a second parallel circuit (CPE_{CT} and R_{CT}) and attributed to the interface and charge transfer between liquid and solid components and any side reactions prior to formation at these interfaces. This process shifts to higher frequencies of about 1000 Hz after formation (presumably due to the finished SEI formation), revealing a fourth process at around 20 kHz, modelled by a third parallel circuit (CPE_{DL} and R_{DL}). This high-frequency contribution can likely be attributed to the electrochemical double layer at the interfaces between liquid electrolyte and active material particles. Any unresolved processes above 1 MHz are again modelled with a simple resistor R_0.

To conclude the discussion on the cell impedance before and after formation: Neither the sodium metal anode nor the $Na_{3.4}Zr_2Si_{2.4}P_{0.6}O_{12}$ separator has a significant impact on the overall cell resistance. This is due to the dominance of the cathode, influenced by both the applied pressure (0.05 MPa or 1 MPa) and component thickness. The resistance change during formation is dominated by a process at intermediate frequencies of roughly 200 Hz to 1500 Hz, attributed to the interfaces between liquid electrolyte and the solid cathode components. At low external pressure (0.05 MPa, cell 1), this resistance contribution increases significantly during formation. In contrast, at a pressure of 1 MPa (cell 2), this resistance decreases.

The formation of cell 2 with reduced cathode and increased separator thickness was again carried out at j = 0.1 mA/cm^2 (equivalent to approximately C/10) in four cycles between 2.6 V and 3.8 V. The resulting voltage, current density and charge are depicted in Figures 7(b) and 8(a). Initially, the cell is charged to 1.18 mAh/cm^2. The first discharge yields 1.11 mAh/cm^2, i.e. 94% of the initial charge is recovered during the first discharge, corresponding to energy densities of $E_{V,\ \mathrm{real}} = (147 \pm 7)$ Wh/l and $E_{m,\ real} = (62 \pm 3)$ Wh/kg. This value corresponds to 84% of the theoretical capacity and energy density when assuming 118 mAh/g for $Na_3V_2(PO_4)_3$. The following three formation cycles all recover more than 99% of the charge during discharge. As expected, the shape of the voltage profile during formation is largely independent of the cathode and separator thickness, as kinetic limitations are not significant at low rates like C/10 (compare Figures 6(a,b) and 8(a,b)).

The overall resistance of cell 2 decreased during the formation phase. This enabled cycling of the cell after formation at higher current densities of j = 0.5 mA/cm^2 (equivalent to approximately $C_{theo}/2$) within the same voltage window as shown in Figure 8(c). In Figure 8(d), capacity retention and Coulombic efficiency of the first 70 cycles are shown. Each cycle achieves a Coulombic efficiency above 99%, with a first discharge of 1.07 mAh/cm^2 (81% of the theoretical cathode capacity) or (142 ± 7) Wh/l on cell level and a 70th discharge of 1.02 mAh/cm^2 (77% of the theoretical cathode capacity) or (136 ± 7) Wh/l on cell level (or (60 ± 3) Wh/kg and (57 ± 3) Wh/kg, respectively.

After every ten cycles, an impedance spectrum was recorded (Figure 9(a)). Interestingly, these recordings have caused dips in the Coulombic efficiency (Figure 8(d)): The voltage amplitude of 25 mV during impedance spectroscopy was sufficient to slightly discharge but not to charge the cell. In Figure 9(a), the spectrum of cell 2 after formation (see Figure 7(b)) is included as 'cycle 0'. While cell degradation is small when quantified by Coulombic efficiency in Figure 8(d), significant increase of cell resistance with increasing cycle number is observed in Figure 9(a). To get a more itemized interpretation of the impedance spectra, the same equivalent circuit was used to fit the data as discussed for Figure 7(b) after formation, assigning current collector polarization (CPE_{CC}), liquid electrolyte ion diffusion (CPE_{LE} and R_{LE}), cathodic electrode/liquid charge transfer resistance (CPE_{CT} and R_{CT}), the electrochemical double layer (CPE_{DL} and R_{DL}) and unresolved high-frequency contributions (R_0). By plotting the fitted values of the four resistances of the equivalent circuit against cycle number (Figure 9(b)), it is hypothesized that the observed degradation in cell

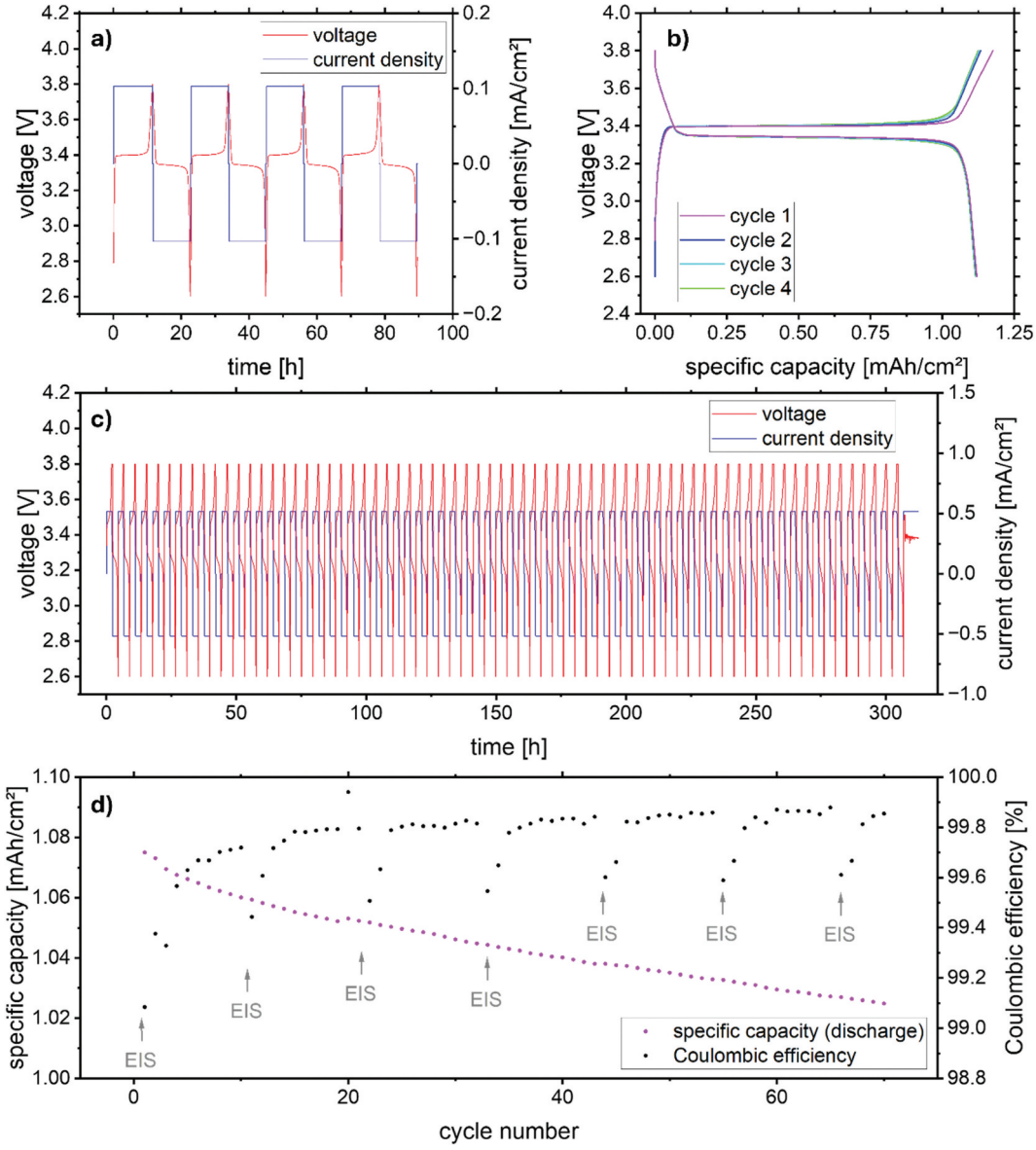

Figure 8. (a) Voltage and current density during formation cycles of the Na-aSSB cell 2 at 0.1 mA/cm^2 ≙ C/10), b) voltage vs. charge during the same measurement, c) cycling of the same cell 2 at 0.5 mA/cm^2 ≙ C/2) after formation, d) discharge capacity and Coulombic efficiency during the same measurement.

resistance is caused by an increase in the resistance contribution associated with the ion diffusion in the liquid electrolyte. Most likely, the volume of liquid electrolyte is slightly decreasing with each cycle by leaking out of the cathode over time. The cell (Figure 1) is sealed in argon atmosphere and uniaxially compressed between two steel plates at a constant pressure of 1 MPa. Leakage is feasible perpendicular to the applied force. This mode of degradation is therefore expected and needs to be resolved in the future, e.g. when using pouch-type cells without voids filled with gas.

However, it was not the increasing resistance that caused the cell to fail after 70 cycles. Instead, a partial short circuit is observed during the 71st charging step in Figure 8(c) due to dendrite formation. This behaviour was observed in all cells that could be successfully cycled due to sufficiently low resistance at current densities of approximately 1 mA/cm^2. It is important to note that cell 2, as shown in Figure 8, displayed dendrite formation significantly later than all other cells of similar assembly. Out of 10 cells studied, it was the only one to survive more than 10 cycles without short-circuiting. The cause of this anomaly is currently under investigation and may be related to the statistical variation of mechanical defects in the ceramic substrates. Dendrites are visible as a grey

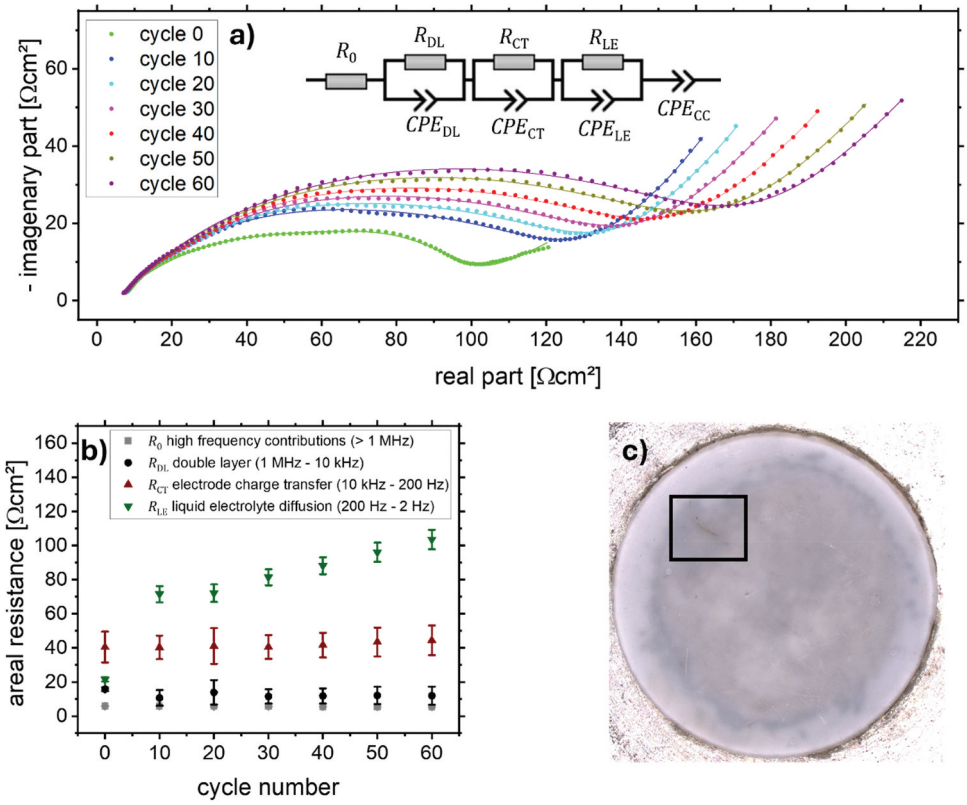

Figure 9. a) Impedance spectra and equivalent circuit of aSSB cell 2 during cycling (see Figure 8(d)). b) Cathode resistance contributions vs. cycle number, as extracted from impedance spectra in Figure 8. Only R_{LE}, shown here with green symbols, increases with increasing cycle number. c) Dendrite in $Na_{3.4}Zr_2Si_{2.4}P_{0.6}O_{12}$ tape after cell failure. Cathode was removed, the sodium anode shows through the translucent separator from the other side, dendrite visible as grey filament in black box.

filament in the $Na_{3.4}Zr_2Si_{2.4}P_{0.6}O_{12}$ tapes after removal of the cathode in a post-mortem analysis (Figure 9(c) depicts an exemplary cell which failed after three cyles). Dendrite formation is most likely caused by mechanical failure of the solid electrolyte, induced by sodium plating in pores and cracks in the vicinity of the sodium metal interface. An in-depth discussion of the mechanical models behind the crack growth in solid electrolytes was conducted by Ning et al. and traced to pores or microcracks close to the metal electrode [34]. Figure 4 reveals such microcracks in the $Na_{3.4}Zr_2Si_{2.4}P_{0.6}O_{12}$ microstructure at grain boundaries. A recent study by Liu et al. has found that modification of the $Na_{3.4}Zr_2Si_{2.4}P_{0.6}O_{12}$ with 2.5 mol% $Na_3LaP_2O_8$ [53] or 2 mol% $LaNbO_4$ [54] reduces grain boundary microcracking and suppresses dendrite formation. Similarly modified $Na_{3.4}Zr_2Si_{2.4}P_{0.6}O_{12}$ materials could be processed via tape casting and be applied to the Na-aSSB concept presented in this study. This is anticipated to significantly enhance both the cycling stability and the maximum charging capability achievable with the cell design and warrants further studies. The observation, that the critical dendrite did not appear in the first charging cycle, but after some cycles at the same current density, is indicative of cell degradation at the sodium- $Na_{3.4}Zr_2Si_{2.4}P_{0.6}O_{12}$ interface as the reason of this effect. This phenomenon has been previously studied in depth by Yang et al. [55] via fluorescence tomography technology. A likely mechanism is the feedback between void accumulation during cell discharge and the subsequent increase of current density at the deteriorating points of electrochemical contact, eventually leading to dendrite penetration as discussed in [56,57].

Discussion of the technological potential regarding energy density

Although several factors need to be considered when evaluating battery concepts, cycling stability and energy density are of primary importance. The previous section addressed the limitations of cycling stability and suggested strategies to mitigate them in future studies; however, the potential for energy density

requires further discussion. A more in depth discussion on the prospects of oxide-based SSBs can be found in [58].

As summarized in Table 1, energy densities of $E_V E_V$ = (239 ± 10) Wh/l and $E_m E_m$ = (118 ± 5) Wh/kg have been achieved with the Na-aSSB cell concept (cell 1). These values are already approaching those of the closest commercial counterparts of the Na-aSSB, which are Na-ion batteries with liquid electrolyte. As of the time of this study, CATL (Contemporary Amperex Technology Co. Limited, China) leads the market with its first-generation Na-ion batteries, offering an energy density of 160 Wh/kg at the cell level [59]. Achieving this target with Na-aSSBs is feasible, as only about 85% of the active material capacity was achieved in cell 1 (based on a theoretical capacity of 118 mAh/g for $Na_3V_2(PO_4)_3$). By optimizing cathode manufacturing to fully activate the cathode, the energy density could therefore potentially reach the theoretical value of approximately 278 Wh/l or 138 Wh/kg (Table 1).

Further improvements could be made by reducing the substantial cathodic porosity from 63% to a level comparable to conventional lithium-ion batteries, which typically have around 30% porosity [60]. This reduction in porosity could decrease $d_{cathode} d_{cathode}$ of cell 1 to (95 ± 5), further elevating the volumetric energy density to approximately 421 Wh/l. Following Equation 5, the gravimetric energy density would also rise to about 184 Wh/kg due to the reduced weight of the liquid electrolyte, surpassing that of first-generation CATL Na-ion batteries.

Energy density can be further increased by eliminating the anodic sodium reservoir, which is currently a (36 ± 5) µm thick layer. Since the cells are assembled in their discharged state, the additional sodium at the anode during assembly is not strictly required for the electrochemical reaction. Although there are challenges associated with the zero-excess sodium metal electrode concept for solid-state batteries [27,29], overcoming these obstacles could increase the energy density of cell 1 to approximately 511 Wh/l or 199 Wh/kg. These energy density values are competitive with CATL's goal of 200 Wh/kg for their second-generation Na-ion batteries [59] and may even exceed those of modern Li-ion batteries if energy density is enhanced further by reducing $d_{separator}$ $d_{separator}$ below 50 µm or by increasing active material loading and/or cell voltage, e.g. by choosing a more advanced active material. Certain layered transition metal oxides show promise in this context [46] and may provide additional benefits related to resource criticality [43] and toxicity [44] by replacing vanadium with other transition metals.

Concluding the discussion of energy density, Na-aSSBs have potential to surpass current Na- and Li-ion batteries in terms of energy density at the cell level. While Li-ion technology is already highly advanced with limited room for improvement, Na-aSSBs could present greater opportunities for enhancement in aspects such as safety, energy density and cycling stability. With further development, they could deliver effective energy storage solutions for a wide array of mobile and stationary applications.

Conclusions

In this study, battery cells were explored, featuring a sodium metal anode, a thin $Na_{3.4}Zr_2Si_{2.4}P_{0.6}O_{12}$ solid electrolyte, and a liquid electrolyte-infiltrated cathode as proof-of-concept for high-energy-density Na-aSSBs.

The $Na_{3.4}Zr_2Si_{2.4}P_{0.6}O_{12}$ separators were fabricated by tape casting and sintering. Their thickness varied from 50 µm to 110 µm. They exhibited a sodium ion conductivity of (1.6 ± 0.3) mS/cm 30°C and activation energies of (0.28 ± 0.01) eV. The tapes were successfully contacted with sodium metal foil using an ultrasonic sonotrode, resulting in interfacial resistances of (1.5 ± 0.6) Ωcm^2 at 30°C. The sodium metal electrode and the $Na_{3.4}Zr_2Si_{2.4}P_{0.6}O_{12}$ separator therefore contribute less than 10 Ωcm^2 to the overall resistance of the aSSB at 30°C.

$Na_3V_2(PO_4)_3$ cathode active material was synthesized and characterized in conventional coin cells, achieving 85% of the theoretical capacity initially and retaining 98% of this value over 500 cycles.

$Na_3V_2(PO_4)_3$/carbon-black composite cathodes were infiltrated with liquid electrolyte and combined with the tape casted $Na_{3.4}Zr_2Si_{2.4}P_{0.6}O_{12}$ separators and sodium metal anodes. During the formation phase, these aSSBs achieved 85% of the theoretical cathode capacity and energy densities as high as (238 ± 10) Wh/l were reached with 50 µm thin separators, among the highest values reported for room temperature sodium battery concepts with oxide ceramic solid electrolytes. Cycling stability and Coulombic efficiencies

exceeding 99% over 70 cycles were demonstrated at currents of 0.5 mA/cm^2 (C/2) at 1 MPa of external pressure with a thinner cathode and 110 µm thin separator.

These investigations revealed five limitations of the Na-aSSB cell concept that should serve as guidelines for further studies:

(1) **Elevated cathode resistance**: The approximately 100 Ωcm^2 resistance of the $Na_3V_2(PO_4)_3$/carbon black composite cathode exceeds the approximately 10 Ωcm^2 resistance of the rest of the cell by one order of magnitude. This high resistance is attributed to an unoptimized cathode microstructure and not related to the metallic sodium and ceramic separator concept. The fabrication of low resistance cathodes including elemental doping and nano structuring is well established in the field of lithium-ion battery technology and can also be applied to Na-aSSBs.
(2) **Further increase in cathode resistance during cycling**: When increasing external pressure to lower the cell resistance, further increase of cell resistance is observed during cycling and is related to changes of the liquid electrolyte, e.g. by liquid electrolyte leaking out of the cathode. This effect is suspected to be reduced in pouch-cell configurations, minimizing gas-filled volumes that avoid loss of liquid electrolyte.
(3) **Mechanical stability and thickness of $Na_{3.4}Zr_2Si_{2.4}P_{0.6}O_{12}$ tapes**: The tape casted $Na_{3.4}Zr_2Si_{2.4}P_{0.6}O_{12}$ separator tends to warp slightly during sintering. This leads to fracture when applying any significant uniaxial pressure to enhance contact between components. Further research into sintering of thin $Na_{3.4}Zr_2Si_{2.4}P_{0.6}O_{12}$ tapes and exploring structural ceramic approaches to decrease defect size and enhance flatness of $Na_{3.4}Zr_2Si_{2.4}P_{0.6}O_{12}$ substrates is required to enable larger electrode areas at significant pressure.
(4) **Dendrite penetration through the solid electrolyte**: Dendrite penetration inevitably led to failure of the battery cell, when degradation of cell resistance as a competing failure mechanism was sufficiently suppressed. This issue most likely prevails as the consequence of porosity and microcracks in the microstructure of the solid electrolyte in combination with pore formation at the Na|ceramic interface during cell discharge. Recent advancements by Liu et al. in modifying $Na_{3.4}Zr_2Si_{2.4}P_{0.6}O_{12}$ with $Na_3LaP_2O_8$ or $LaNbO_4$ show promise for mitigating dendrite formation by achieving denser microstructures, which can be applied to thin tape-cast substrates [53,54].
(5) **Energy Density**: The achieved values of (238 ± 10) Wh/l and (118 ± 5) Wh/kg indicate significant potential for optimization. To enhance the energy density of Na-aSSBs, strategies include optimizing the cathode microstructure to increase the percentage of activated $Na_3V_2(PO_4)_3$ and reduce porosity. Additionally, efforts should be made to minimize anodic sodium excess, ideally aiming for complete removal [27,29]. Successfully implementing all three strategies could raise the Na-aSSB energy density to 511 Wh/l and 199 Wh/kg. Further enhancements may be achieved by utilizing active materials with higher capacity [46] or by reducing the $Na_{3.4}Zr_2Si_{2.4}P_{0.6}O_{12}$ thickness to below 50 µm.

In conclusion, the successful demonstration of the Na-aSSB with a thin ceramic $Na_{3.4}Zr_2Si_{2.4}P_{0.6}O_{12}$ separator at the laboratory scale paves the way for further studies. The identified challenges provide a base for research aiming at developing Na-aSSB cells that can achieve performance levels at least comparable to modern Na- and Li-ion batteries.

Acknowledgments

The authors thank M.-T. Gerhards for preparation of the Na3.4Zr2Si2.4P0.6O12 powder. The financial support from the German Federal Ministry of Education and Research is gratefully acknowledged.

Disclosure statement

No potential conflict of interest was reported by the author(s).

Funding

This work was funded by the German Federal Ministry of Education and Research (BMBF) within the projects HeNa (support codes 13XP0390A and 13XP0390B) and NASS (support code 13XP0490B).

ORCID

Ansgar Lowack http://orcid.org/0000-0002-5589-7455

CRediT authorship contribution statement

Ansgar Lowack: Conceptualization, Data curation, Formal analysis, Investigation, Visualization, Writing – original draft. **Rafael Anton**: Conceptualization, Data curation, Investigation, Writing – Review & Editing. **Dörte Wagner**: Conceptualization, Data curation, Investigation, Writing – Review & Editing. **Monika Bhardwaj**: Conceptualization, Investigation, Data curation, Writing – Review & Editing. **Stephan Prünte**: Conceptualization, Investigation, Data curation, Writing – Review & Editing. **Enkhtsetseg Dashjav**: Conceptualization, Investigation, Visualization, Data curation, Writing – Review & Editing. **Kristian Nikolowski**: Conceptualization, Funding acquisition, Writing – Review & Editing, Supervision. **Frank Tietz**: Conceptualization, Investigation, Funding acquisition, Writing – Review & Editing, Project administration. **Katja Wätzig**: Conceptualization, Writing – Review & Editing, Supervision. **Mihails Kusnezoff**: Conceptualization, Funding acquisition, Writing – Review & Editing, Project administration, Supervision. **Mareike Partsch**: Conceptualization, Funding acquisition, Writing – Review & Editing, Supervision. **Alexander Michaelis**: Conceptualization, Funding acquisition, Supervision.

Data availability statement

Data is made available by the authors upon reasonable request.

References

[1] Nayak PK, Yang L, Brehm W, et al. From lithium-ion to sodium-ion batteries: advantages, challenges, and surprises. Angew Chem Int Ed. 2018;57(1):102–120. doi: 10.1002/anie.201703772
[2] Hasegawa G, Hayashi K. Nasicon-based all-solid-state Na-ion batteries: a perspective on manufacturing via tape-casting process. APL Energy. 2023;1(2):020902. doi: 10.1063/5.0151559
[3] Goodenough JB, Hong HY-P, Kafalas JA. Fast Na^+ -ion transport in skeleton structures. Mater Res Bull. 1976;11(2):203–220. doi: 10.1016/0025-5408(76)90077-5
[4] Ma Q, Tsai C-L, Wei X-K, et al. Room temperature demonstration of a sodium superionic conductor with grain conductivity in excess of 0.01 S cm^{-1} and its primary applications in symmetric battery cells. J Mater Chem A. 2019;7(13):7766–7776. doi: 10.1039/C9TA00048H
[5] Ortmann T, Burkhardt S, Eckhardt JK, et al. Kinetics and pore formation of the sodium metal anode on NASICON-type $Na_{3.4}Zr_2Si_{2.4}P_{0.6}O_{12}$ for sodium solid-state batteries. Adv Energy Mater. 2023;13(8):2202712. doi: 10.1002/aenm.202202712
[6] Chen S, Wu C, Shen L, et al. Challenges and perspectives for NASICON-type electrode materials for advanced sodium-ion batteries. Adv Mater. 2017;29(48):1700431. doi: 10.1002/adma.201700431
[7] Ma Q, Tietz F. Solid-state electrolyte materials for sodium batteries: towards practical applications. ChemElectrochem. 2020;7(13):2693–2713. doi: 10.1002/celc.202000164
[8] Darjazi H, Falco M, Colò F, et al. Electrolytes for sodium-ion batteries: the current transition from liquid to solid and hybrid systems. Adv Mater. 2024;36(15):2313572. doi: 10.1002/adma.202313572
[9] Zhao J, Wang X, Wei T, et al. Current challenges and perspectives of garnet-based solid-state electrolytes. J Energy Storage. 2023;68:107693. doi: 10.1016/j.est.2023.107693
[10] Janek J, Zeier WG. A solid future for battery development. Nat Energy. 2016;1(9):16141. doi: 10.1038/nenergy.2016.141
[11] Li JG, Liang XS, Yin CG, et al. Preparation of NASICON disk by tape casting and its CO_2 sensing properties. Key Eng Mater. 2013;537:134–139. doi: 10.4028/www.scientific.net/KEM.537.134
[12] Okubo K, Wang H, Hayashi K, et al. A dense NASICON sheet prepared by tape-casting and low temperature sintering. Electrochim Acta. 2018;278:176–181. doi: 10.1016/j.electacta.2018.05.020
[13] Han X, Wang J, Liu Y, et al. Low-temperature brazing strategy for high voltage $Na_4MnCr(PO_4)_3$ cathode-based solid-state sodium-ion batteries. ACS Appl Mater Interface. 2025;17(15):19086–19092. doi: 10.1021/acsami.4c22739

[14] Li Y, Li M, Sun Z, et al. Recent advance on NASICON electrolyte in solid-state sodium metal batteries. Energy Storage Mater. 2023;56:582–599. doi: 10.1016/j.ensm.2023.01.047
[15] Li Y, Sun C, Sun Z, et al. Boosting Na-O affinity in $Na_3Zr_2Si_2PO_{12}$ electrolyte promises highly rechargeable solid-state sodium batteries. Adv Funct Mater. 2024;34(31):2403937. doi: 10.1002/adfm.202403937
[16] Li Y, Wang Z, Sun C, et al. Na-K interlayer driven Na-NASICON solid-state batteries. Adv Funct Mater. 2025;35(5):2425995. doi: 10.1002/adfm.202425995
[17] Ni Q, Xiong Y, Sun Z, et al. Rechargeable sodium solid-state battery enabled by in situ formed Na-K interphase. Adv Energy Mater. 2023;13(22):2300271. doi: 10.1002/aenm.202300271
[18] Sun C, Li Y, Sun Z, et al. Ferroelectric interface for efficient sodium metal cycling in anode-free solid-state batteries. Mater Today. 2024;80:395–405. doi: 10.1016/j.mattod.2024.09.018
[19] Suo J, Zhao Q, Tian H, et al. Designing a quasi-liquid alloy interface for solid Na-ion battery. ACS Nano. 2023;17(11):10229–10235. doi: 10.1021/acsnano.3c00397
[20] Jaschin PW, Tang CR, Wachsman ED. High-rate cycling in 3D dual-doped NASICON architectures toward room-temperature sodium-metal-anode solid-state batteries. Energy Environ Sci. 2024;17(2):727–737. doi: 10.1039/D3EE03879C
[21] Jaschin PW, Tang CR, Wachsman ED. Fast charging and low temperature capabilities of sodium solid-state batteries enabled by thin NASICON bilayer architecture. ACS Energy Lett. 2025;10(5):2610–2616. doi: 10.1021/acsenergylett.5c00575
[22] Rosen M, Mahioui S, Schwab C, et al. Tape casting of NASICON-based separators with high conductivity for Na all-solid-state batteries. Electrochem. 2025;6(1):5. doi: 10.3390/electrochem6010005
[23] Yi E, Shen H, Heywood S, et al. All-solid-state batteries using rationally designed garnet electrolyte frameworks. ACS Appl Energy Mater. 2020;3(1):170–175. doi: 10.1021/acsaem.9b02101
[24] Barai P, Fuchs T, Trevisanello E, et al. Study of void formation at the lithium|solid electrolyte interface. Chem Mater. 2024;36(5):2245–2258. doi: 10.1021/acs.chemmater.3c01708
[25] Hou M, Zhou Y, Liang F, et al. Research progress of solid electrolyte interphase for sodium metal anodes. Chem Eng J. 2023;475:146227. doi: 10.1016/j.cej.2023.146227
[26] Uchida Y, Hasegawa G, Shima K, et al. Insights into sodium ion transfer at the Na/NASICON interface improved by uniaxial compression. ACS Appl Energy Mater. 2019;2(4):2913–2920. doi: 10.1021/acsaem.9b00250
[27] Ortmann T, Fuchs T, Eckhardt JK, et al. Deposition of sodium metal at the copper-NaSICON interface for reservoir-free solid-state sodium batteries. Adv Energy Mater. 2024;14(8):2302729. doi: 10.1002/aenm.202302729
[28] Hüttl J, Seidl C, Auer H, et al. Ultra-low LPS/LLZO interfacial resistance – towards stable hybrid solid-state batteries with Li-metal anodes. Energy Storage Mater. 2021;40:259–267. doi: 10.1016/j.ensm.2021.05.020
[29] Lowack A, Grun P, Anton R, et al. Sputtered zero-excess electrodes with metallic seed layers for solid-state sodium batteries. Batteries Superca. 2024;8(5):e202400364. doi: 10.1002/batt.202400364
[30] Eckhardt JK, Kremer S, Merola L, et al. Heteroionic interfaces in hybrid solid-state batteries—current constriction at the interface between different solid electrolytes. ACS Appl Mater Interface. 2024;16(15):18222–18235. doi: 10.1021/acsami.4c01808
[31] Eckhardt JK, Klar PJ, Janek J, et al. Interplay of dynamic constriction and interface morphology between reversible metal anode and solid electrolyte in solid state batteries. ACS Appl Mater Interface. 2022;14(31):35545–35554. doi: 10.1021/acsami.2c07077
[32] Geng L, Xue D, Yao J, et al. Morphodynamics of dendrite growth in alumina based all solid-state sodium metal batteries. Energy Environ Sci. 2023;16(6):2658–2668. doi: 10.1039/D3EE00237C
[33] Virkar AV, Viswanathan L. Sodium penetration in rapid ion conductors. J Am Ceramic Soc. 1979;62(9–10):528–529. doi: 10.1111/j.1151-2916.1979.tb19123.x
[34] Ning Z, Li G, Melvin DLR, et al. Dendrite initiation and propagation in lithium metal solid-state batteries. Nature. 2023;618(7964):287–293. doi: 10.1038/s41586-023-05970-4
[35] Liu Y, Xu X, Jiao X, et al. Role of interfacial defects on electro-chemo-mechanical failure of solid-state electrolyte. Adv Mater. 2023;35(29):2301152. doi: 10.1002/adma.202301152
[36] Wolfenstine J, Go W, Kim Y, et al. Mechanical properties of NaSICON: a brief review. Ionics. 2023;29(1):1–8. doi: 10.1007/s11581-022-04820-z
[37] Wang X, Chen J, Wang D, et al. Improving the alkali metal electrode/inorganic solid electrolyte contact via room-temperature ultrasound solid welding. Nat Commun. 2021;12(1):7109. doi: 10.1038/s41467-021-27473-4
[38] Soundaraj PV, Dashjav E, Grüner D, et al. Influence of carbon content on the ionic and electronic conductivities of dense $Na_3V_2(PO_4)_3$/C composites. J Power Sources Adv. 2024;26:100144. doi: 10.1016/j.powera.2024.100144
[39] Si L, Yuan Z, Hu L, et al. Uniform and continuous carbon coated sodium vanadium phosphate cathode materials for sodium-ion battery. J Power Sources. 2014;272:880–885. doi: 10.1016/j.jpowsour.2014.09.046
[40] Kashif Razzaq H, Yang C-C, Norhaffis Mustafa M, et al. Progress in multi-electron sodium vanadium phosphate cathode for emerging sodium-ion batteries. Prog Mater Sci. 2025;151:101424. doi: 10.1016/j.pmatsci.2024.101424

[41] Chen Y, Xu Y, Sun X, et al. Effect of Al substitution on the enhanced electrochemical performance and strong structure stability of $Na_3V_2(PO_4)_3$/C composite cathode for sodium-ion batteries. J Power Sources. 2018;375:82–92. doi: 10.1016/j.jpowsour.2017.11.043
[42] Cao R, Mishra K, Li X, et al. Enabling room temperature sodium metal batteries. Nano Energy. 2016;30:825–830. doi: 10.1016/j.nanoen.2016.09.013
[43] Rodby KE, Jaffe RL, Olivetti EA, et al. Materials availability and supply chain considerations for vanadium in grid-scale redox flow batteries. J Power Sources. 2023;560:232605. doi: 10.1016/j.jpowsour.2022.232605
[44] Wnuk E. Mobility, bioavailability, and toxicity of vanadium regulated by physicochemical and biological properties of the soil. J Soil Sci Plant Nutr. 2023;23(2):1386–1396. doi: 10.1007/s42729-023-01130-9
[45] Xiao Y, Xiao J, Zhao H, et al. Prussian blue analogues for sodium-ion battery cathodes: a review of mechanistic insights, current challenges, and future pathways. Small. 2024;20(31):2401957. doi: 10.1002/smll.202401957
[46] Phogat P, Dey S, Wan M. Comprehensive review of sodium-ion batteries: principles, materials, performance, challenges, and future perspectives. Mater Sci Eng B. 2025;312:117870. doi: 10.1016/j.mseb.2024.117870
[47] Janek J, Zeier WG. Challenges in speeding up solid-state battery development. Nat Energy. 2023;8(3):230–240. doi: 10.1038/s41560-023-01208-9
[48] Woolley HM, Vargas-Barbosa NM. Hybrid solid electrolyte-liquid electrolyte systems for (almost) solid-state batteries: why, how, and where to? J Mater Chem A. 2023;11(3):1083–1097. doi: 10.1039/D2TA02179J
[49] Ma Q, Guin M, Naqash S, et al. Scandium-substituted $Na_3Zr_2(SiO_4)_2(PO_4)$ prepared by a solution-assisted solid-state reaction method as sodium-ion conductors. Chem Mater. 2016;28(13):4821–4828. doi: 10.1021/acs.chemmater.6b02059
[50] Anton R, Lowack A, Wagner D, et al. Thin solid-electrolytes with sodium conductive phase $Na_5RSi_4O_{12}$ (R = Yb, Y, Gd, Sm) made via tape-casting. J Eur Ceramic Soc. 2025;45(3):117163. doi: 10.1016/j.jeurceramsoc.2024.117163
[51] Dashjav E, Bhardwaj M, Gerhards M-T, et al. Phase evolution of NaSICON materials during temperature-dependent conventional and cold sintering. ACS Appl Energy Mater. 2025;8(15):11373–11381. doi: 10.1021/acsaem.5c01521
[52] Dashjav E, Gerhards M-T, Klein F, et al. Phase-field determination of NaSICON materials in the quaternary system Na_2O-P_2O_5-SiO_2-ZrO_2: ii. Glass-ceramics and the phantom of excessive vacancy formation. Next Energy. 2024;4:100130. doi: 10.1016/j.nxener.2024.100130
[53] Liu L, Ma Q, Zhou X, et al. Simultaneously improving sodium ionic conductivity and dendrite behavior of NASICON ceramics by grain-boundary modification. J Power Sources. 2025;626:235773. doi: 10.1016/j.jpowsour.2024.235773
[54] Liu L, Liu Y, Zhou X, et al. Nominal lanthanum niobate, a versatile additive for reducing grain boundary resistance in conductive ceramics. Adv Energy Mater. 2025;15(18):2404985. doi: 10.1002/aenm.202404985
[55] Yang Y, Chen H, Zhang J, et al. Imaging dendrite growth in solid-state sodium batteries using fluorescence tomography technology. Sci Adv. 2024;10(47). doi: 10.1126/sciadv.adr0676
[56] Lowack A, Nakum Y, Anton R, et al. Quantifying sodium dendrite formation in $Na_5SmSi_4O_{12}$ solid electrolytes. Batteries Superca. 2025:2500279. doi: 10.1002/batt.202500279
[57] Fuchs T, Haslam CG, Richter FH, et al. Evaluating the use of critical current density tests of symmetric lithium transference cells with solid electrolytes. Adv Energy Mater. 2023;13(34):2302383. doi: 10.1002/aenm.202302383
[58] Schnell J, Tietz F, Singer C, et al. Prospects of production technologies and manufacturing costs of oxide-based all-solid-state lithium batteries. Energy Environ Sci. 2019;12(6):1818–1833. doi: 10.1039/C8EE02692K
[59] CATL. Catl unveils its latest breakthrough technology by releasing its first generation of sodium-ion batteries. 2021. catl.com. https://www.catl.com/en/news/665.html
[60] Boyce AM, Lu X, Brett DJ, et al. Exploring the influence of porosity and thickness on lithium-ion battery electrodes using an image-based model. J Power Sources. 2022;542:231779. doi: 10.1016/j.jpowsour.2022.231779